SCIENTIFIC REPORTS

OPEN

SUBJECT AREAS:
CHEMICAL BIOLOGY
CHEMICAL SYNTHESIS

Received
14 August 2013

Accepted
12 August 2014

Published
29 August 2014

Correspondence and requests for materials should be addressed to G.E.J.P. (g.poinern@murdoch.edu.au)

The synthesis, characterisation and *in vivo* study of a bioceramic for potential tissue regeneration applications

Gérrard Eddy Jai Poinern[1], Ravi Krishna Brundavanam[1], Xuan Thi Le[1], Philip K. Nicholls[2], Martin A. Cake[3] & Derek Fawcett[1]

[1]Murdoch Applied Nanotechnology Research Group, Department of Physics, Energy Studies and Nanotechnology, School of Engineering and Energy, Murdoch University, Murdoch, Western Australia 6150, Australia, [2]School of Veterinary and Life Sciences, Molecular and Biomedical Sciences, Murdoch University, Murdoch, Western Australia 6150, Australia, [3]School of Veterinary and Life Sciences, College of Veterinary, Murdoch University, Murdoch, Western Australia 6150, Australia.

Hydroxyapatite (HAP) is a biocompatible ceramic that is currently used in a number of current biomedical applications. Recently, nanometre scale forms of HAP have attracted considerable interest due to their close similarity to the inorganic mineral component of the bone matrix found in humans. In this study ultrafine nanometre scale HAP powders were prepared via a wet precipitation method under the influence of ultrasonic irradiation. The resulting powders were compacted and sintered to form a series of ceramic pellets with a sponge-like structure with varying density and porosity. The crystalline structure, size and morphology of the powders and the porous ceramic pellets were investigated using advanced characterization techniques. The pellets demonstrated good biocompatibility, including mixed cell colonisation and matrix deposition, *in vivo* following surgical implantation into sheep *M. latissimus dorsi.*

Every year millions of people worldwide require a bone transplant and the preferred bone replacement procedure involves the use of an autograft material (patient's own bone) since it displays excellent biocompatibility, osteogenic properties and delivers bone forming cells to the implant site. Today, the medical use of autografts is well established with good clinical outcomes and as a result the procedure is considered the gold standard for bone transplantation. However, problems such as donor site morbidity and the limited source of potential donor sites have caused researchers in the field to look for alternative sources of bone tissue[1–4]. The use of alternative materials such as allogenic bone grafts (sourced from another donor) generally results in a significant response from the body's immune system, while disease transmission resulting from this procedure is potentially a serious side effect[5]. Furthermore, obtaining bone tissue for an allograft procedure is complicated by medical, ethical and legal concerns. Moreover, both autograft and allograft procedures also suffer from a limited supply of high quality bone tissue for suitable medical use.

An attractive alternative to natural bone grafts is to create synthetic materials that can be formed into implants or scaffolds for bone regeneration. The engineered scaffold needs to create a porous architectural structure, which effectively replicates the various physical, chemical and mechanical properties found in natural bone tissue. Therefore, the scaffold material needs be biologically compatible, *i.e.* it should be nontoxic to the body tissues[6–8], non-immunogenic, and have a degradation rate synchronized with the formation of new tissues[9]. The advantage of the balanced degradation rate is that it will allow the invading cells to steadily colonise the scaffold and at the same time permit the formation of blood vessels necessary for the delivery of nutrients to the forming bone tissues. Other important properties of the scaffold should include: 1) an internal architecture consisting of suitably sized interconnecting pores that mimic the structure of trabecular bone[10,11]; 2) the internal surface area of the inter-connecting pore structure should be optimised for maximum cell coverage; 3) the surface chemistry of the scaffold material should maximize cell and tissue adhesion; 4) the material should be capable of being sterilized; and 5) material should also be mechanically strong enough to withstanding normal physical loading encountered *in vivo*[12–14].

Due to the close chemical similarity of synthetic hydroxyapatite (HAP) to the natural form found in the inorganic component of the bone matrix, there have been extensive research efforts into employing synthetic HAP as a bone substitute in a number of clinical applications such as bone augmentation, coating metal implants and filling components in both bone and teeth[15–19]. The most important factor that must be addressed to achieve a successful clinical outcome is the biological compatibility of the material used to construct the implant or scaffold.

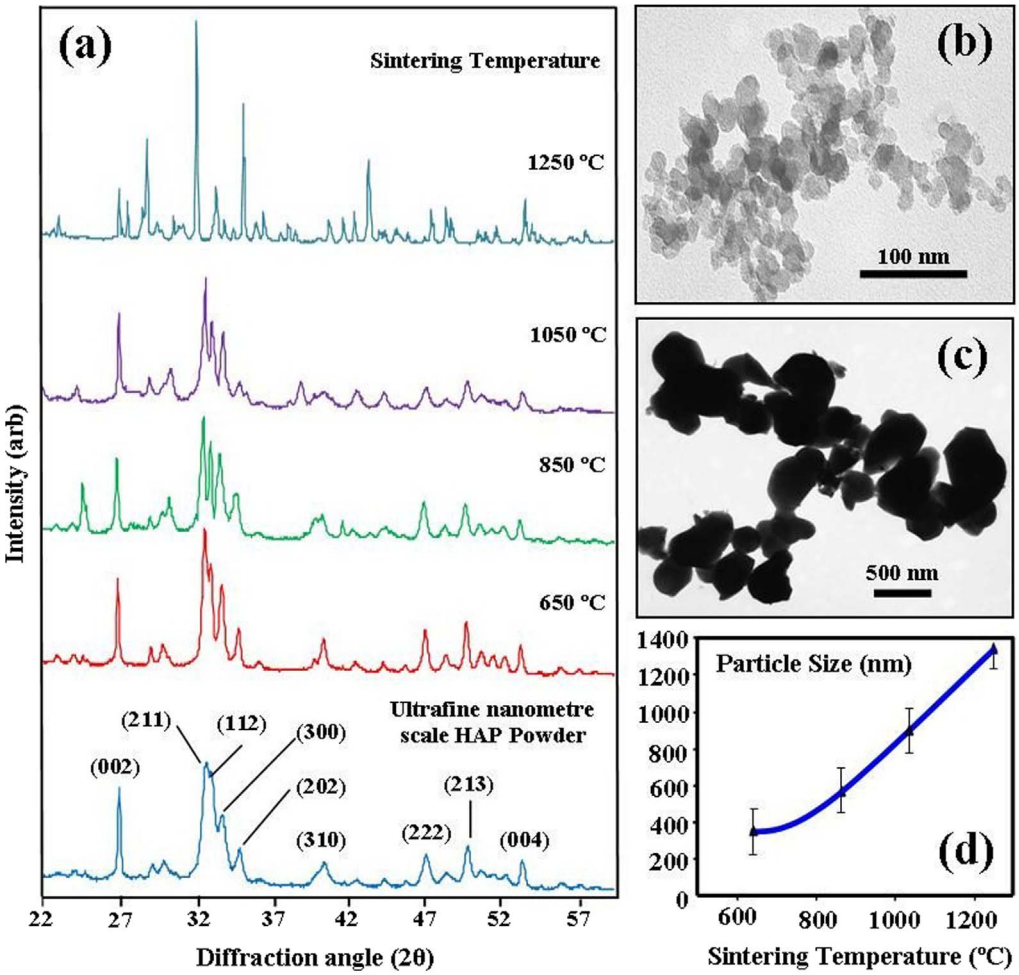

Figure 1 | XRD and TEM analysis. (a) XRD spectrum of synthesised nano-HAP powder and sample powders taken from thermally treated pellets at various sintering temperatures (b) TEM micrograph of synthesized nanometre scale HAP powder (c) TEM micrograph of particles sintered at 850°C (d) a graph showing particle growth with increasing sintering temperature.

For example, the material should not induce any cytotoxicity, immunological reactions, and inflammatory responses from the body[6–8]. The four main features that make synthetic HAP attractive for clinical applications are: 1) it has good biocompatibility with tissues such as skin, muscle and gums[20]; 2) its biodegradability *in situ* is slow; 3) it provides good osteoconductivity; and 4) it offers good osteoinductivity capabilities[16,21,22]. Furthermore, due to its excellent biocompatibility, dispersed nanometre scale HAP and similar calcium phosphate particles have found new and novel medical applications such as carriers in biological systems for the transfer of nucleic acids and therapeutic drugs[23,24]. It was because of these highly attractive features of synthetic HAP that it was selected as the scaffold material for present study. Therefore, the three aims of this study were firstly to form a set of ceramic pellets with a sponge- like structure with varying density and porosity from a nanometre scale HAP powder and micrometre scale porogen. Secondly, the physical and chemical properties of pellets were studied using advanced characterization techniques and finally using a pilot *in vivo* study to investigate the biocompatibility of the pellets for potential tissue regeneration applications by surgical implantation into sheep *M. latissimus dorsi*.

Results

XRD spectroscopy analysis. XRD pattern analysis was used to identify the purity and crystalline size of the synthesised nanometre scale HAP powders and the particle size of the HAP based ceramic pellets sintered at temperatures of 650°C, 850°C, 1050°C and 1250°C, as shown in Figure 1 (a). Analysis of all XRD patterns, except the 1250°C pattern revealed the presence of crystalline nanometre scale HAP phases. These phases were found to be consistent with the phases listed in the ICDD database, with the main (h k l) indices for nano-HAP: (002), (211), (300), (202), (130), (002), (222) and (213) being indicated. However, the diffraction pattern for the 1250°C sample indicated that significant decomposition of the HAP phase had taken place. The decomposition of HAP in atmospheric air at elevated temperatures was reported and discussed by Liao *et al*[25]. Their study revealed that during gradual heating from 1000 to 1360°C, HAP steadily releases its OH^- ions and transforms into crystalline oxyhydroxyapatite (OHAP). Above 1360°C, Liao *et al* also found that the OHAP would decompose into a tetra calcium phosphate (TTCP) and α-tricalcium phosphate (α-TCP) phase. The products seen in the 1250°C XRD pattern consist of a significantly reduced HAP component, sizeable amounts of β-tricalcium phosphate (β-TCP) and the presence of small amounts of potassium calcium hydrogen phosphate and potassium calcium phosphate (Detailed XRD pattern is presented in supplementary information).

The crystalline size, $t_{(hkl)}$, of the ultrafine HAP powders and samples from the sintered HAP based pellets was calculated from the respective XRD patterns using the Debye-Scherrer equation[26–28]

$$t_{(hkl)} = \frac{0.9\lambda}{B\cos\theta_{(hkl)}} \quad (1)$$

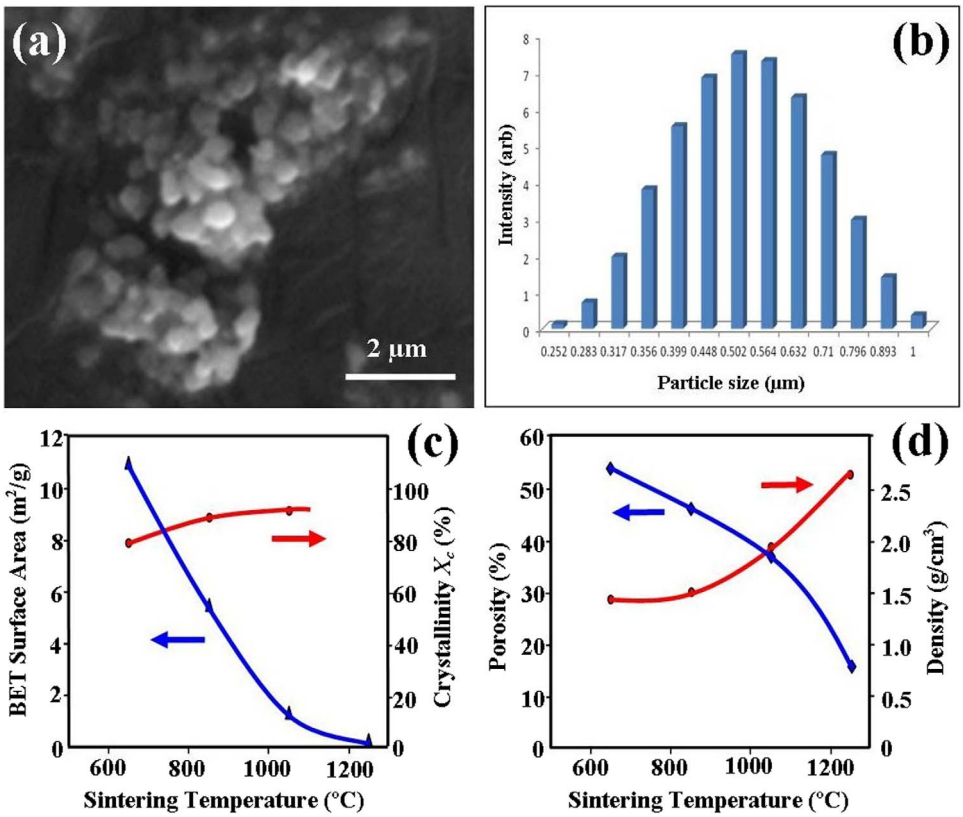

Figure 2 | Particle size analyses. (a) FESEM image of HAP sample sintered at 850°C (b) a typical particle size profile showing particle size distribution for 850°C. The effect of increasing sintering temperature on: (c) Surface area and crystallinity and (d) Porosity and density.

where, λ is the wavelength of the monochromatic X-ray beam, B is the Full Width at Half Maximum (FWHM) of the peak at the maximum intensity, $\theta_{(hkl)}$ is the peak diffraction angle that satisfies Bragg's law for the (h k l) plane and $t_{(hkl)}$ is the crystallite size. The crystallite size calculated from the (002) reflection peak for the powder gave a mean value of 30 nm, while the mean particle size for the sintered samples ranged from 323 nm for the 650°C up to 1224 nm for the 1250°C sample. The degree of crystallinity and the subsequent growth in particle size has a significant influence on the material's properties such as density and porosity. Hence, the percentage crystallinity of the material was calculated using the equation proposed by Landi *et.al*[29], see equation 2.

$$X_C = 1 - (V_{112-300}/I_{300}) \quad (2)$$

where X_C is the percentage crystallinity of the material, $V_{112\text{-}300}$ is the intensity of the trough between (112) and (300) peaks and I_{300} is the intensity of (300) peak. The crystallinity of the powder was estimated to be 48.17%. Subsequent analysis revealed that the sintering process promoted both particle growth and enhancement of crystallinity in the pellets as seen in Figures 1 (d) and 2 (c).

FESEM and TEM microscopy analysis. The size and morphology of both the nanometre scale HAP powders and the structure of various sintered pellets was investigated using both TEM and FESEM. A typical TEM micrograph of the ultrafine powder is presented in Figure 1 (b) and reveals the presence of a spherical particle morphology, which is similar to the particle morphologies reported in the literature[30–34]. The mean particle size determined from TEM analysis was found to be 28 ± 5 nm, which was comparable to the mean value of 30 nm calculated from the XRD spectra. Both TEM and FESEM techniques were used to determine the size and morphology of the particles produced in the pellets during the sintering process. A typical TEM micrograph taken of particles produced during sintering at 850°C is presented in Figure 1 (c), while the results of a particle size distribution analysis for the 850°C samples are presented in Figure 2 (b). The particle analysis revealed a mean particle size of 538 nm ± 120 nm, which closely matched the results of TEM (550 nm ± 150 nm) and FESEM (Figure 2 (a)) with a mean particle size of 518 nm ± 140 nm. Analysis of all pellets sintered at various sintering temperatures (650°C, 850°C, 1050°C and 1250°C) revealed that the increased temperatures produced an increase in particle size and a morphological structure becoming more angular, cubic and rectangular in nature. The results of the particle size analysis were similar to findings of the XRD analysis with the mean particle size ranging from 376 nm for the 650°C up to 1318 nm for the 1250°C (Figure 1 (d)). However, at the higher sintering temperature of 1250°C, the morphology and much greater particle size diversity confirmed HAP decomposition identified in the XRD analysis.

The FT-IR spectroscopy analysis. Inspection of a typical FT-IR spectrum of synthesized ultrafine powder is presented in Figure 3 (b) and reveals the presence of several bands associated with nanometre scale HAP. Starting from the right hand side of the spectrum, the first two bands encountered are 564 cm^{-1} and 601 cm^{-1}, which are the result of v_4 vibrations being produced by the O-P-O mode. The next two bands located at 725 cm^{-1} and 832 cm^{-1}, (each with a low transmittance) are associated with the carbonate group and clearly indicate the presence of carbonates in the samples. The 961 cm^{-1} band results from the v_1 symmetric stretching vibrations of the P-O mode. While the very strong peaks located at 1032 cm^{-1} and 1092 cm^{-1} correspond to the PO_4^{3-} functional group (P-O mode) and the weaker peak at 1384 cm^{-1} corresponds to the CO^{2-}_3 functional group. The carbonate formation most likely results from the interaction between atmospheric carbon dioxide and the alkaline HAP precursor solution during the synthesis

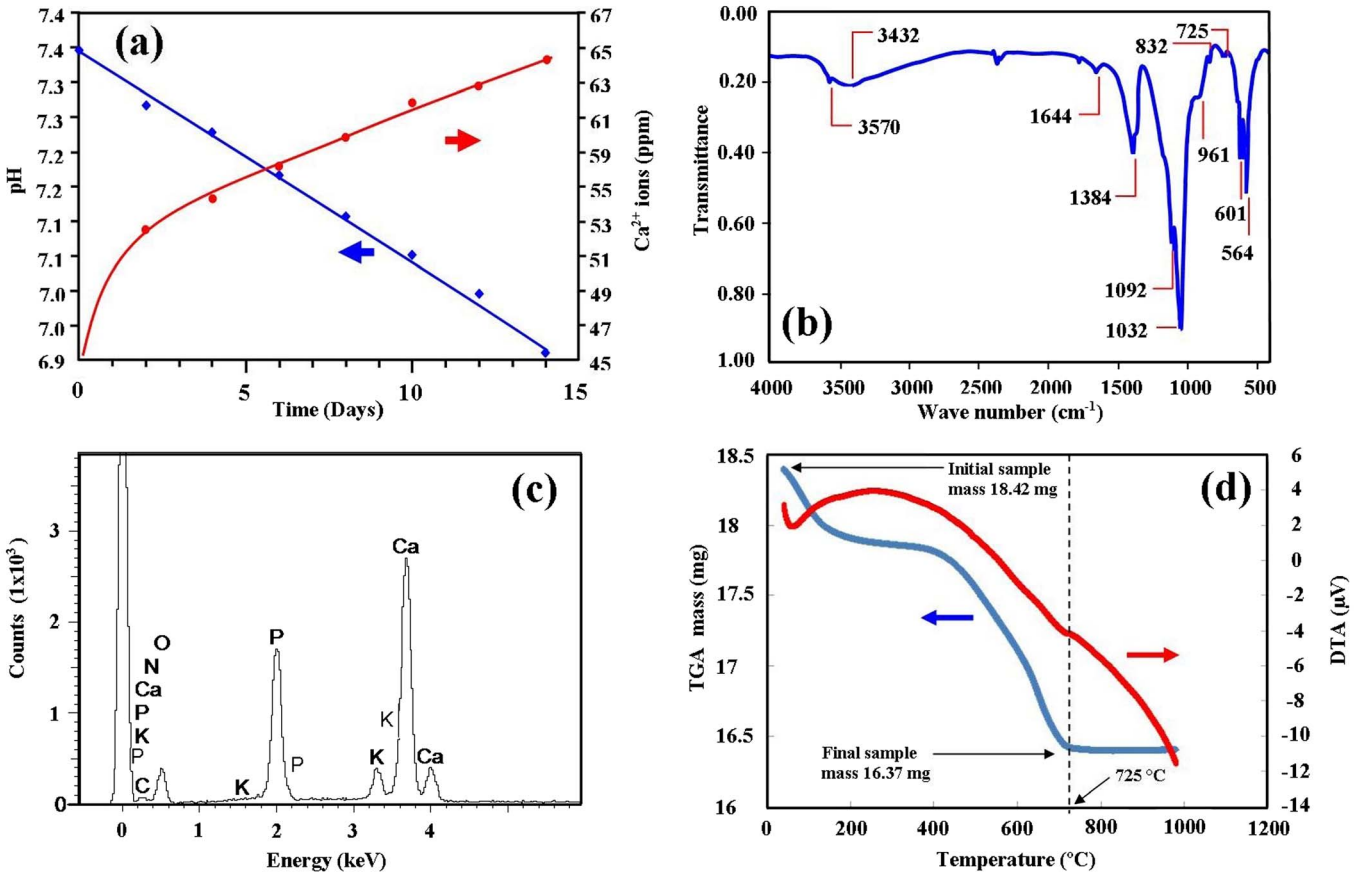

Figure 3 | Physical and chemical property analyses. (a) In vitro assessment: variation of pH and the release of Ca^{2+} ions from a nano-HAP powder immersed in a PBS solution over a 14 day period (b) FT-IR spectrum of a synthesised and thermally treated nano-HAP powder (c) EDS spectrum of a synthesised nano-HAP powder used to confirm chemical composition and calculate the Ca/P ratio (d) TGA and DTA thermograph of the synthesised nano-HAP powder.

process[35–37]. The smaller peak located at 1644 cm^{-1} also corresponds to a $CO^{2-}{}_3$ group. The band located at 3432 cm^{-1} indicates the presence of absorbed water, while the weak peak at 3570 cm^{-1} corresponds to the vibrations of OH^- ions in the HAP lattice. The results of the FT-IR analysis clearly indicate that the synthesized ultrafine powders are HAP.

Energy dispersive X-ray spectroscopy analysis. The EDS spectrum presented in Figure 3 (c) reveals the presence of two dominant peaks, namely Ca and P, while on the left hand side of the spectrum, to a lesser extent is an oxygen peak. Calculation of the Ca/P ratio from the EDS spectrum gives a value of 1.656, which is very close to the stoichiometric value of 1.67 used in the ultrasonic process to create HAP. The close agreement of the Ca/P (approx. 0.84%) not only confirms the presence of HAP, but also confirms that the HAP powders produced are of high quality and confirms the results of the XRD analysis.

Differential thermal and Thermal Gravimetric Analysis. Analysis of the DTA thermograph presented in Figure 3 (d) reveals that there were no exothermic or endothermic reactions taking place over the 24 to 980°C temperature range. Furthermore, no phase transformations occurred over this temperature range, which confirmed the physical and chemical stability of the HAP powder sample and was similar to the results of Farzadi *et al*[38]. Figure 3 (d) presents a typical TGA thermograph of a powder sample and reveals a decreasing trend in sample mass resulting from water loss. The initial sample mass was 18.42 mg and the final mass at the end of the heating cycle was 16.37 mg, indicating a water loss of 2.05 mg (11.3%). Analysis of the thermograph revealed a three-stage water loss profile over the temperature range. In the first stage, there was a 2.6% mass loss observed, indicating the evaporation of surface moisture and absorbed water. During the second stage, there was a 1% mass loss observed, while in the final stage there was a sharp 7.7% mass loss resulting from the loss of lattice water. From 725°C onwards, there was no further mass loss from the sample indicating the high thermal stability of the HAP powder up to about 1000°C.

***In vitro* assessment.** Dissolution under physiological conditions of nanometre scale HAP powder samples was carried out in a phosphate buffered saline (PBS) solution at 37°C with an initial solution pH of 7.40. The initial pH of 7.40 was selected because it is the mean pH value of the extracellular fluid, which is tightly regulated by buffers to remain within the narrow range of 7.35 to 7.45. After immersion of sample into the PBS solution, both the pH and Ca^{2+} ion concentration values were recorded at regular time intervals over a 14 day period as presented in Figure 3 (a). During this period solution pH steadily decreased from 7.40 to 6.98 (5.7%) indicating that the solution was becoming less alkaline. However, natural pH regulation by blood based buffers *in vivo* would significantly restrict any variation. During the same assessment period Ca^{2+} ion dissolution from the sample steadily increases up to a maximum value of 63 ppm at the end of the test period as seen in Figure 3 (a). The low dissolution rate of Ca^{2+} ions into the PBS solution suggests that the relatively small release of ions is not likely to cause any adverse effects in the body's ability to maintain its calcium balance; since osteoclasts routinely resorb bone tissue and return calcium back to the extracellular fluid.

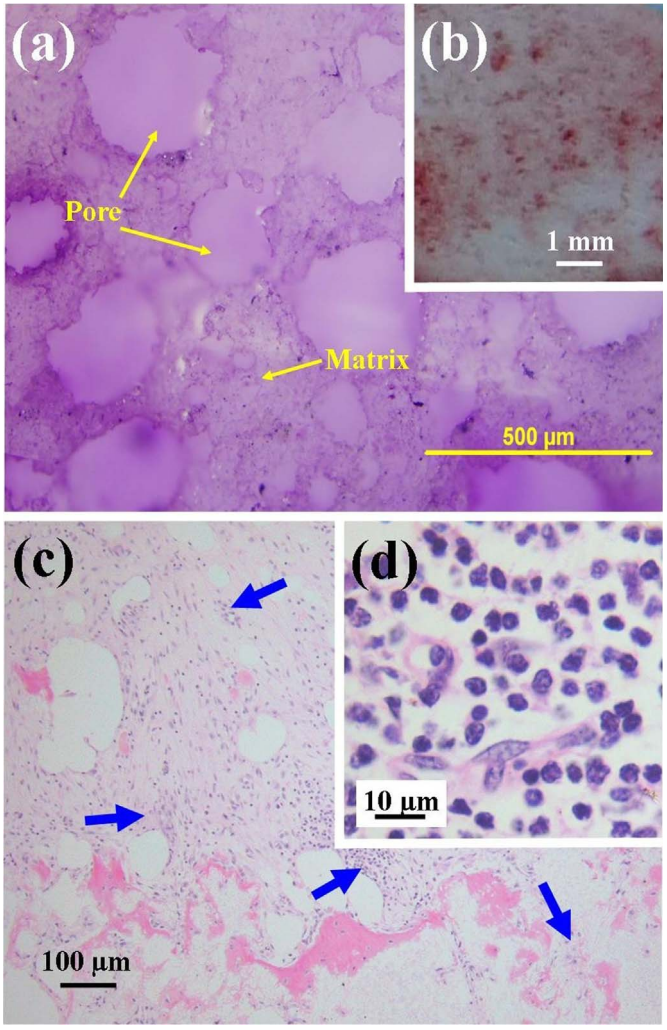

Figure 4 | Analysis of porosity and cell infiltration. (a) A typical surface image of macro-pores found in ceramic pellets before implantation (b) A typical surface image of a reclaimed pellet showing infiltration and blood-staining suggestive of porosity (c) a micrograph showing dense cell clusters (arrowheads) throughout the body of the implanted pellet and Inset (d) shows details of lymphocytes with dark round nucleus and scant cytoplasm, and occasional spindle shaped fibroblastic cells (850°C: H&E. 12 weeks).

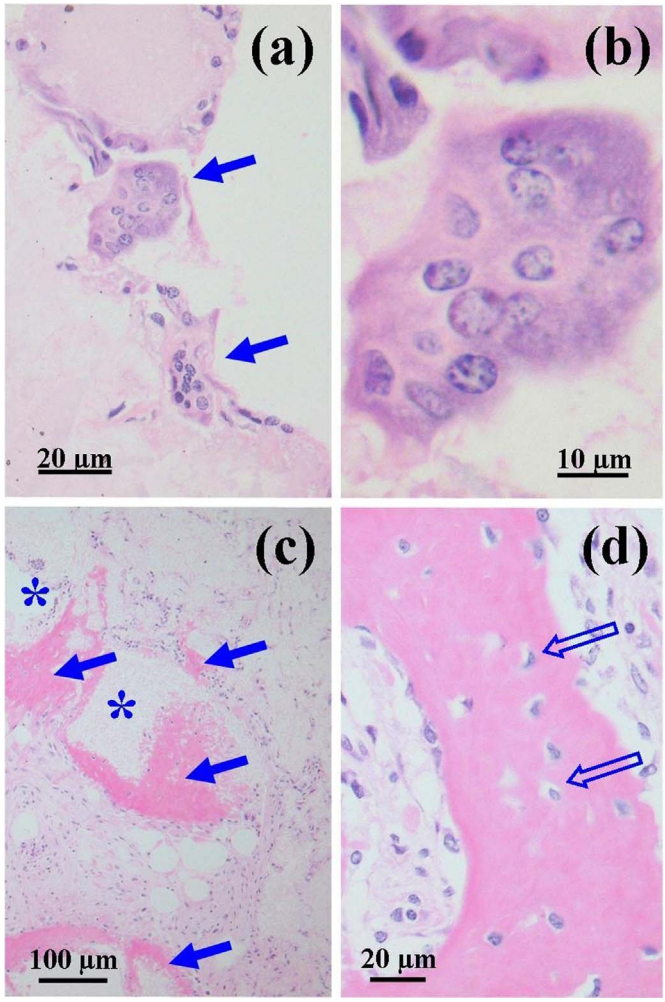

Figure 5 | Typical cells present and cellular colonisation of implant. (a) Multinucleate giant cells (arrows) at edge of a typical HAP implant (b) enlargement of an individual multinucleate giant cell under ×100 oil immersion objective (H&E. 12 weeks) (c) dense eosinophilic matrix (bone matrix – solid arrows) within the body of the implant, amongst non colonised areas of implant (*), and surrounded by fibrous tissue (d) shows an area of bone matrix in which individual cells (osteocytes – open arrows) are present within small cavities (lacunae) (850°C: H&E. 12 weeks).

Physical property analysis. The results of Brunauer-Emmett-Teller (BET) surface area analysis, porosity and density studies of the powder based pellets sintered at temperatures of 650°C, 850°C, 1050°C and 1250°C are presented in Figures 2 (c) and 2(d). The largest surface area (10.977 m^2/g), the highest porosity (53.02%) and lowest density (1.449 g/cm^3) were recorded for the lowest sintering temperature of 650°C. While the lowest surface area (1.137 m^2/g), lowest open porosity (36.78%) and highest density (1.952 g/cm^3) were recorded for the sintering temperature 1050°C. The lowest sintering temperature of 650°C had the lowest density and highest porosity, which tended to produce an open porous structure. Increasing the sintering temperature promoted particle growth and produced a significantly reduction in both surface area and porosity. However, as previously discussed, the sintering temperature of 1250°C resulted in significant HAP decomposition.

***In vivo* assessment.** Pellet implantation into sheep *M. latissimus dorsi* was well tolerated and elicited no pain, gross swelling or visible immune response. Significant adherence to the surrounding capsule was found in some specimens, with increased adherence at 12 weeks and also for higher sintered temperature pellets (850°C, 1050°C and 1250°C); in several cases a strongly adherent fibrous 'pseudo-periosteum' was noted. Most pellets grossly showed infiltrated blood-staining suggestive of porosity and vascular invasion as seen in Figure 4 (b). Histological studies of the surrounding tissue capsule showed healthy granulation tissue and myofibre regeneration, with mild focal lymphohistiocytic inflammation mainly related to areas of fat necrosis (*i.e.* typical of a healing surgical wound). Pellets reclaimed at the end of the 4th week revealed the presence of multinucleated giant cells at the surface of the pellet as seen in Figures 5 (a) and (b). Optical microscopy observations revealed that the internal three-dimensional porous structure of the pellets provided an attractive environment for cells to infiltrate and colonise as seen in Figure 4 (c). Branching channels deep within the body of the pellet were in places, lined by flat squamous cells resembling endothelia (Figures 6 (c) and (d)). By the end of week 12 both connective tissues and bone matrix were being formed throughout the pellet, which clearly indicated that the HAP powder based pellets were highly biocompatible. Collagen formations were identified as a fibrillar eosinophilic matrix amongst spindle shaped cells (fibroblasts), having a positive stain

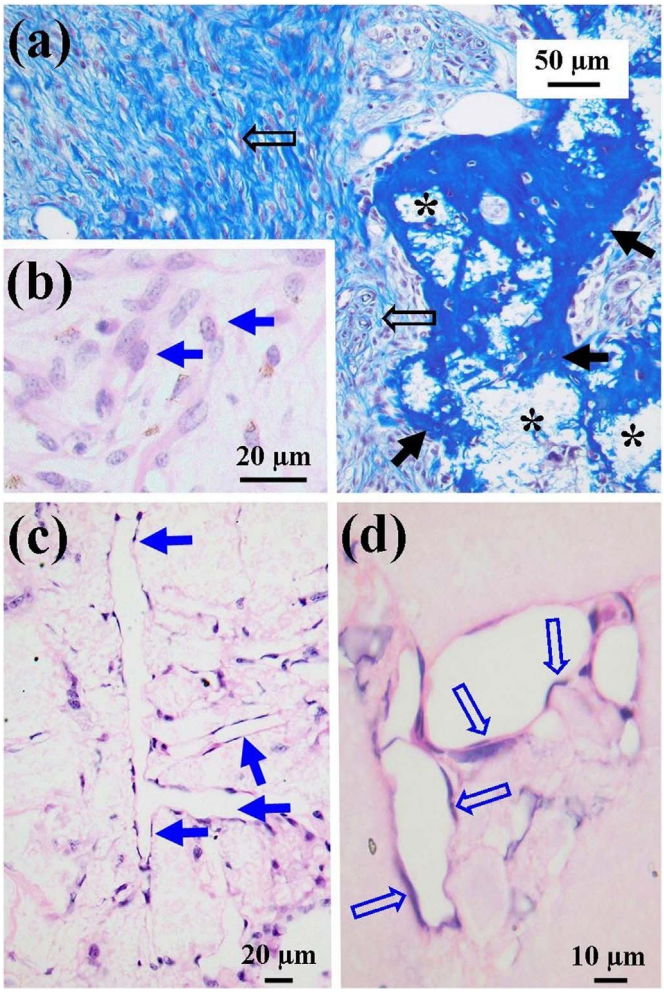

Figure 6 | Tissue in-growth and vessel-like structures. (a) Tissue in-growth, within the body of the implant, including areas of bone (solid arrows) and fibrous tissue (open arrows) amongst small foci of non colonised implant matrix (*) (Martius scarlet blue. 12 weeks) (b) Inset shows fibroblastic cells amongst fibrous stroma (arrowheads) (H&E. 12 weeks) (c) tissue in-growth within the body of the implant, in the form of branching vessel-like structures (solid arrows) (d) endothelial-like cells (open arrows) lining the apparent vessels (850°C: H&E. 4 weeks).

with Martius scarlet blue[39] (Figure 6 (a)), and with a birefringent appearance under crossed polarising filters. Bone matrix (Figures 5 (c), 5 (d) and 6 (a)) was identified as a condensed (hyalinised) eosinophilic matrix, containing abundant collagen fibres positively stained (blue) with Martius scarlet blue. The bone matrix (Figure 6 (a)) showed bifringence under crossed polarizing filters, and was found to be populated by scattered cells (osteocytes) with small cavities (lacunae) typical of bone (Figure 5 (d)). Other tissue components that could be mistaken for osteoid include fibrin, amyloid and degenerate muscle fibres. These were eliminated because they stain red, rather than blue, with the Martius scarlet blue stain, and would not have the woven, weakly-birefringent appearance seen under polarised light[40]. Some reclaimed pellets had scattered deposits of round cells with scant cytoplasm (lymphocytes), at both superficial and deep locations (multifocally), including the deepest regions of the pellet (Figure 4 (c) and (d)).

Discussion

The ceramic based HAP scaffolds with sponge-like pore structure were manufactured from nanometre scale HAP powders composed of spherical 30 nm particles and spherical shaped stearic acid (~350 µm in diameter), which was used as both binding agent and porogen. The HAP powders were synthesized using a wet chemical method incorporating ultrasonic irradiation previously developed and optimized by the authors since the technique allowed particle size selection[41,42]. The powders were characterized using XRD and TEM to determine crystallinity, particle size, and phases present. EDS and FT-IR were used to determine the Ca/P ratio and identify functional groups present in the samples, while both TGA and DTA analysis confirmed the thermal stability of the HAP powders up to 1000°C. HAP is conventionally sintered at high temperatures (~1000°C) and results in grain growth and densification to form a solid bioceramic[43]. Lower temperatures generally produce ceramics with smaller grain sizes, but are generally unstable and rapidly deteriorate under load. However, studies have found that grain size directly influences the cellular interactions and functions of both osteoblasts and osteclasts[44–46]. It is for this reason that a number of studies have looked at producing bioceramics sintered at temperatures ranging from 650 to 900°C[47,48], while other studies have looked at producing bioceramics without sintering[49]. Because of the strong influence of particle size on cell-material interactions, the sintering temperature in this study started with the lowest feasible temperature of 650°C and was raised up to 1250°C. All pellets sintered at 650°C, 850°C, 1050°C and 1250°C for 2 h in air were structurally stable and therefore suitable for surgical implantation into sheep *M. latissimus dorsi*. However, analysis of XRD patterns for samples taken from pellets sintered at 1250°C revealed significant HAP decomposition. The decomposition resulted from the release of OH^- ions from the HAP lattice structure occurring above 1000°C[23] and produced significant amounts of β-tricalcium phosphate (β-TCP) in addition to the presence of remaining HAP. Also detected at 1250°C was the presence of small amounts of potassium calcium hydrogen phosphate and potassium calcium phosphate. The source of the potassium originated from the potassium di-hydrogen phosphate used during the synthesis of the HAP. The indexed XRD pattern of the products produced at 1250°C can be found in the supplementary information.

After sintering, the resulting sponge-like scaffolds sintered at 650, 850 and 1050°C were HAP, structurally stable and displayed increasing trends in particle size and density. Meanwhile, porosity and BET surface area of the pellets decreased with increasing temperature. Examination of microscopic images from various pellets reveals a matrix with a wide range of pores sizes. For example, Figure 4 (a) presents a typical surface image of the 850°C pellet showing a variety of pore sizes. The largest pore diameter seen was 350 µm, with a wide variety of smaller pores diameters down to 75 µm. The pore size is of particular biological importance since cells must be able to infiltrate and colonise the scaffold for effective tissue regeneration to take place. The ideal pore size recommended for cellular growth and bone in-growth ranges from 100 to 1000 µm[43], with some researchers even suggesting that pore sizes of at least 300 µm are needed for effective bone tissue formation and blood capillary development[50]. Therefore, cell infiltration and subsequent colonisation of a scaffold are essential parameters for effective tissue regeneration and ultimately lead to a successful clinical outcome. The reclaimed pellets all showed signs of infiltrated blood-staining suggestive of porosity and vascular invasion, with the lower sintering temperatures of 650°C and 850°C showing the most staining. For example, Figure 4 (b) shows wide spread blood-staining over the surface of the 650°C pellet indicating its porous structure. Furthermore, histological inspection of the micro-section images of the various pellets reveal a pore structure with a large surface area to bulk volume ratio, with extensive interconnecting networks of flow channels throughout the matrix. This sponge-like pore structure, (as confirmed by the density and porosity investigations) which mimics trabecular bone is comparable to structures produced by other researchers and has similar properties such

as large pores and extensive porosities[51,52]. The importance of pore size and inter-connectivity is crucial in biomedical applications: allowing cell migration, vascularisation, promoting the diffusion of nutrients and the removal of metabolic wastes resulting from cellular activities[53]. All reclaimed pellets show signs of cell colonisation and cellular activity, with the 650°C and 850°C pellets showing the most colonisation activity. The colonisation activity seen in these two pellets was the direct result of the high porosities (650°C (53%) and 850°C (47%)) and the inter-connecting channel structure formed during sintering. Pellets sintered at 1050°C were found to have porosity of around 37% and also displayed a similar channel structure, which permitted cell infiltration and colonisation to a lesser extent.

At the end of week 12, histological studies of all sintered pellets (650°C, 850°C, 1050°C and 1250°C) revealed that cells could be seen throughout the scaffold matrix (Figure 4 (c)), which suggests that the cells are travelling through the matrix via the inter-connecting pore structure. This inter-connecting structure of pore channels consists of different pore sizes and geometries. Pore diameters as large as 150 μm can be seen in Figure 4 (c), while in Figure 6 (d) diameters as small as 20 μm are present. In particular, cells could be seen lining the channel-like pores in the inner regions of the scaffold (Figure 6 (c) and (d)) proving that the inter-connecting pore structure was suitable for *in vivo* cell colonisation. Furthermore, the presence of new collagen and large areas of new bone could be seen throughout the internal matrix of the various pellets including infiltration by lymphocytes in some samples (Figure 4 (d)). Also seen were numerous scattered cells (osteocytes) with small cavities (lacunae) present in the bony matrix (Figure 5 (d)). The ability to support collagenous and bony matrix deposition, as well as to allow connective tissue and inflammatory cell infiltration, seen in this *in vivo* study, clearly demonstrates the clinical potential of HAP powder based ceramic pellets for hard tissue regeneration applications. The stimulation of bone deposition, especially within the surrounding muscle environment without direct contact with host bone, is an interesting finding. Bone formation within muscle is seen in the clinical condition myositis ossificans, typically secondary to muscle injury, or as heterotopic bone due to the effects of bone morphogenetic protein[54]. Osteoinduction within muscle has been reported with other solid materials, such as zinc tricalcium phosphate, in the absence of added bone morphogenetic protein[55].

The results of the histological investigations have shown that HAP based pellets are capable of being used as an effective tissue scaffold. The presence of several cell types, including the deposition of a new bone matrix, suggests that this scaffold has the potential to be used as a bone graft. The study has shown that cells were capable of infiltrating the extensive 3-D inter-connecting pore structure and colonise the pellet scaffold. All reclaimed HAP based pellets (650°C, 850°C and 1050°C) at week 12 showed extensive cellular activity and supported collagenous and bony matrix deposition, as well allowing connective tissue and inflammatory cells to infiltrate. The presence of different cell types, other than bone cells also confirms the scaffold's wider biocompatibility towards other cells. Based on the encouraging results of this pilot study, further work is planned to improve and match the physical and mechanical properties of the pellets with those of natural bone tissue. Once these properties have been achieved, further *in vivo* studies, will be carried out to establish the feasibility of using this scaffold for bone grafts.

Methods

Scaffold material and manufacturing. Combining nanometre scale HAP powder with Stearic acid, which acted as both binding agent and porogen, formed the micrometre scale porous structure of the scaffold. An extensive description of the production route for synthesizing nanometre scale HAP powders and porous bioceramic materials by the authors is given elsewhere[42,56]. In brief, HAP synthesis begins by adding a 40 mL solution of 0.32 M calcium nitrate tetra-hydrate into a small glass beaker. The pH of the solution is then adjusted to 9.0 by slowly adding and mixing approximately 2.5 mL of ammonium hydroxide (all chemicals supplied by Chem-Supply, Australia). Once the pH is stabilized, the solution was then subjected to ultrasonic irradiation for a 1 h using a Hielscher UP50H 950 W Ultrasound Processor. After the first hour, a 60 mL solution of 0.19 M potassium di-hydrogen phosphate was slowly added drop-wise into the first solution while undergoing a second hour of ultrasonic irradiation. During the second hour, the pH of the solution was monitored and maintained at 9.0 and the Calcium/Phosphate [Ca/P] ratio maintained at 1.67. At the end of the second hour, the resulting solution underwent centrifugation (15,000 g) for 20 minutes at room temperature. The resultant white precipitate sample was then washed, centrifuged for a further 10 minutes and then deposited into a fused silica crucible before being thermally treated at 100% power for 40 minutes in a domestic microwave (1100 W at 2450 MHz-LG® Australia). At the end of the thermal treatment the sample was ball milled until all the agglomerations were removed to form an ultrafine nano-HAP powder. Meanwhile, stearic acid (supplied by Sigma-Aldrich, Australia) was ball milled to produce a spherically shaped particle with a mean particle size of 350 μm. Then a mixture of HAP and stearic acid [1% wt. of Stearic acid to 99% wt HAP] was mechanical mixed together for 2 h. The blended powder was then cold compressed in a cylindrical mould by a manually operated single action axial hydraulic ram pressurized to 70 MPa and maintained at this pressure for 1 h to produce a standard pellet size (diameter 18.60 ± 0.05 mm and a length of 18.30 ± 0.05 mm). The pellets were then sintered in a programmable high temperature muffle furnace [Model 60 SL, Kiln Manufacturers of Western Australia] at treatment temperatures of 650°C, 850°C, 1050°C and 1250°C for a period of 2 h.

Advanced characterization techniques. Powder X-ray diffraction (XRD) spectroscopy was recorded at room temperature, using a Siemens D500 series diffractometer [Cu K_α = 1.5406 Å radiation source] operating at 40 kV and 30 mA. The diffraction patterns were collected over a 2θ range of 20° to 60° with an incremental step size of 0.04° using flat plane geometry with 2 second acquisition time for each scan. The powder XRD spectrum was used to identify the purity of the final nano-HAP powders and the phases present. The size of the particles in the powders were calculated using the Debye-Scherrer equation [Equation 1] from the respective XRD patterns, while a bright field Transmission Electron Microscopy (TEM) study was carried out using a Phillips CM-100 Electron microscope operating at 80 kV to confirm particle size and morphology. In addition, the fraction of crystalline phase (X_c) present in the sintered pellets at various temperatures was calculated using the crystallinity equation proposed by Landi *et al*[29] [Equation 2]. Field Emission Scanning Electron Microscopy (FESEM) techniques were used to investigate the size, morphological and macro-structural features of the samples. All micrographs were taken using a high resolution FESEM [Zeiss 1555 VP-FESEM] at 3 kV with a 30 μm aperture operating under a pressure of 1.333×10^{-10} mbar. In addition, the micrometre scale particle size distribution of HAP found in the sintered samples was found by using a Malvern Mastersizer® 3000 (Malvern Instruments Ltd, UK). From the analysis of the particle size distribution data a general error was determined and applied to the individual measurements. Pore diameter and distribution throughout the pellet cross-sections were investigated using an Olympus BX51 compound microscope (Olympus Optical Co. Ltd., Tokyo, Japan) fitted with a DP 70 camera attachment.

Fourier Transform Infrared (FT-IR) spectroscopy investigations were carried out using a Bruker Optics IFS 66 series FT-IR spectrometer. The KBr pellet technique was used, in which 2 g of nano-HAP powder was mixed with 5–10 g of spectroscopic grade KBr and then compressed at around 15 kPa to form a disk. All FT-IR spectra data was recorded in the range from 400 cm^{-1} to 4000 cm^{-1} in steps of 4 cm^{-1}. The resulting spectra were then analysed using the OMNIC® software package. Energy Dispersive Spectroscopy (EDS) was used to provide an elemental analysis of the samples using an Oxford Instruments energy dispersive system (133 eV resolution), via a 10 mm^2 SATW detector. The analysis was carried out to verify the results of the XRD analysis and to calculate the Ca/P ratio of the synthesised nano-HAP powders. Thermal Gravimetric Analysis (TGA) and Differential Thermal Analysis (DTA) were carried out using a Perkin Elmer Simultaneous Thermal Analyzer STA 6000. The scan cycle started from room temperature and steadily increased temperature at a rate of 15°C/min up to a maximum temperature of 980°C. TGA was used to find weight loss during the heating cycle, while DTA was used to investigate potential exothermic or endothermic reactions and potential phase transformations.

Physical property characterization. The density and porosity were determined firstly by dimensional and mass measurements and secondly by Archimedes' principle. Dimensions of each pellet were measured using a micrometer (Mitutoyo M210-25) and their respective weights measured using an Ohaus PA214C microbalance. The porosity was then determined from the difference in the theoretical density of HAP (3.16 g/cm^3) and the apparent density. The second technique determined porosity by immersing a previously vacuum dried pellet into a small beaker containing a solution of Milli-Q® water (18.3 $M\Omega\,cm^{-1}$) produced by an ultrapure water system [Barnstead Ultrapure Water System D11931; Thermo Scientific, Dubuque, IA] for a period of 2 hours. The pellet was then removed from the solution, weighed and then submerged back into the Milli-Q® water and its weight was measured. The Brunauer-Emmett-Teller (BET) surface area measurements of the nano-HAP powders were carried out by the Australian Commonwealth Scientific and Industrial Research Organisation's (CSIRO) Particle Analysis Services laboratory (PAS) in Perth, Western Australia.

***In vitro* assessment.** Dissolution under physiological conditions of the ultrafine nano-HAP powders was carried out in a phosphate buffered saline (PBS) solution, with the pH adjusted to 7.4. The solution was then sterilized by autoclaving at 120°C for 20 minutes, before being allowed to cool to room temperature and then stored. Powder samples were added to the PBS solution, which was then gently stirred and maintained at 37°C for the study period. Both the solution pH and Ca^{2+} ion concentration levels were monitored over the 14 day study period. The pH of each sample solution was measured using a Smith Electronics Q1416 metre. The sample solution was then filtered using a 0.2 μm membrane and then centrifuged at 15,000 g for 20 minutes. An equal amount of PBS was then added to the stock solution to maintain the initial volume. After filtration and centrifuging, the Ca^{2+} ion concentration in the sample solution was measured using a Varian Vista Axial CCD: ICP-AES inductively coupled plasma atomic emission spectrometer.

***In vivo* assessment and histology.** An *in vivo* implantation study was carried out in sheep (3–4 year old non-pregnant Merino ewes) with the approval of Murdoch University's Animal Ethics Committee (R2298/09), and all experiments were conducted in accordance with the Australian National Health and Medical Research Council's (NHMRC) Code of Practice for the care and use of animals for scientific purposes. In accordance with the ethical principles of the Code (reduce/re-use), the sheep were simultaneously used in an unrelated trial involving surgery of the stifle joints (AEC R2042/07). Under general anaesthetic and using full sterile procedure, four steam-sterilised nano-HAP pellets each of different sinter temperatures (650, 850, 1050 and 1250°C) were surgically implanted into adjacent pockets created by blunt dissection within the right *M. latissimus dorsi* muscle of the four sheep. The muscle pocket, subcutis and skin were then closed using synthetic absorbable sutures and antibiotic prophylaxis provided (1 g cephalexin sodium). After recovery, the sheep were accommodated on free-range pasture with some supplementary grain feeding. Pellets were harvested at 4 weeks and 12 weeks post-implantation (2 sheep per time point), after humane euthanasia for the above-mentioned projects. Reclaimed pellets were carefully dissected and manually tested for adherence to the surrounding tissue capsule. The samples were fixed in 10% neutral-buffered formalin and processed for routine histology. The pellets and any adherent tissue were fixed in formalin before being routinely processed through paraffin wax and sectioned at 4 μm thickness. For light microscopy and polarising light microscopy, dissected pellets were fixed in formalin, decalcified in 5% nitric acid, processed routinely through paraffin wax, and sectioned at 4 μm before staining with haematoxylin and eosin, or Martius scarlet blue. A specialist veterinary pathologist evaluated the sections qualitatively and with some subjective semi-quantitative assessments.

1. Kao, S. T. & Scott, D. D. A Review of Bone Substitutes. *Oral. Maxillofac. Surg. Clin. North Am.* **19**, 513–521 (2007).
2. Brems, J. J. Role of bone graft substitutes for glenoid bone defects. *J. Shoulder Elbow Surg.* **16**, S282–S285 (2007).
3. LaPrade, R. F. & Botker, J. C. Donor site morbidity after osteochondral autograft transfer procedures. *Arthroscopy.* **20**, e69–e73 (2004).
4. Mischkowski, R. A. *et al.* Donor site morbidity of ear cartilage autographs. *Plast. Reconstr. Surg.* **121**, 79–87 (2008).
5. Ng, V. Risk of disease transmission with bone allograft. *Orthopaedics.* **35**, 679–681 (2012).
6. Veronese, F. M. *et al.* PEG–doxorubicin conjugates: influence of polymer structure on drug release, in vitro cytotoxicity, bio-distribution, and antitumor activity. *Bioconjug. Chem.* **16**, 775–784 (2005).
7. Wong, H. L. *et al.* A new polymer–lipid hybrid nanoparticle system increases cytotoxicity of doxorubicin against multidrug-resistant human breast cancer cells. *Pharm. Res.* **23**, 1574–1585 (2006).
8. Timmer, M. D., Shin, H. & Horch, R. A. In vitro cytotoxicity of injectable and biodegradable poly (propylene fumarate)-based networks: unreacted macromers, cross-linked networks, and degradation products. *Biomacromolecules.* **4**, 1026–1033 (2003).
9. Song, C. *et al.* Facilitation of hematopoietic recovery by bone grafts with intra-bone marrow-bone marrow transplantation. *Immunobiology.* **213**, 455–468 (2008).
10. Habibovic, P. *et al.* 3D microenvironment as essential element for osteoinduction by biomaterials. *Biomaterials.* **26**, 3565–3575 (2005).
11. Ripamonti, U. [Smart biomaterials with intrinsic osteoinductivity: Geometric control of bone differentiation] *In bone engineering* [Davies, J. E. (ed.)] [215–222] (EM Squared Incorporation, Toronto, 2000).
12. Schindler, O. S. *et al.* Use of a novel bone graft substitute in peri-articular bone tumours of the knee. *The Knee.* **14**, 458–464 (2007).
13. Murugan, R. & Ramakrishna, S. Development of nanocomposites for bone grafting. *Comp. Sci. Technol.* **65**, 2385–2406 (2005).
14. Galois, I. & Mainard, D. Bone ingrowth into porous ceramics with different pore sizes: an experimental study. *Acta. Orthop. Belg.* **70**, 598–603 (2004).
15. Hutmacher, D. W. *et al.* State of the art and future directions of scaffold-based bone engineering from a biomaterials perspective. *J. Tissue. Eng. Regen. Med.* **1**, 245–260 (2007).
16. Habraken, W. J. E. M., Wolke, J. G. C. & Jansen, J. A. Ceramic composites as matrices and scaffolds for drug delivery in tissue engineering. *Adv. Drug. Deli. Rev.* **59**, 234–248 (2007).
17. Taniguchi, M. *et al.* The clinical application of intravenous catheter with percutaneous device made of sintered hydroxyapatite. *Jpn. J. Artif. Organs.* **20**, 460–464 (1991).
18. Silva, R. V. *et al.* The use of hydroxyapatite and autogenous cancellous bone grafts to repair bone defects in rats. *Inter. J. Oral & Maxillofacial Surg.* **34**, 178–184 (2005).
19. Stoch, A. *et al.* Sol-gel derived hydroxyapatite coatings on titanium and its alloy Ti6Al4V. *J. Mol. Struct.* **744**, 633–640 (2005).
20. Kalita, S. J., Bhardwaj, A. & Bhatt, H. A. Nano-crystalline calcium phosphate ceramics in biomedical engineering. *Mater. Sci. Eng. C.* **27**, 441–449 (2007).
21. Blom, A. Which scaffold for which application. *Curr. Orthop.* **21**, 280–287 (2007).
22. Habibovic, P. & de Groot, K. Osteoinductive biomaterials-properties and relevance in bone repair. *J. Tissue. Eng. Regen. Med.* **1**, 25–32 (2007).
23. Epple, M. *et al.* Application of calcium phosphate nanoparticles in biomedicine. *J. Mater.Chem.* **20**, 18–23 (2010).
24. Hagmeyer, D. *et al.* Self-assembly of calcium phosphate nanoparticles into hollow spheres induced by dissolved amino acids. *J. Mater. Chem.* **21**, 9219–9223 (2011).
25. Liao, C.-J. *et al.* Thermal decomposition and reconstitution of hydroxyapatite in air atmosphere. *Biomaterials.* **20**, 1807–1813 (1999).
26. Danilchenko, S. N. *et al.* Determination of the bone mineral crystallite size and lattice strain from diffraction line broadening. *Cryst. Res. Technol.* **37**, 1234–1240 (2002).
27. Klug, H. P. & Alexander, L. E. *X-ray diffraction procedures for polycrystallite and amorphous materials* (Wiley, New York, 1974).
28. Barrett, C. S. *et al. Advances in X-ray analysis* (Plenum Press, New York, 1986).
29. Landi, E. *et al.* Densification behaviour and mechanisms of synthetic hydroxyapatites. *J. Eur. Ceramic. Soc.* **20**, 2377–2387 (2000).
30. Zhuo, Z.-H. *et al.* Controllable synthesis of hydroxyapatite nanocrystals via a dendrimer-assisted hydrothermal process. *Materials Research Bulletin.* **42**, 1611–1618 (2007).
31. Aryal, S. *et al.* Synthesis and characterisation of hydroxyapatite using carbon nanotubes as a nano-matrix. *Scripta Materialia.* **54**, 131–135 (2006).
32. Saeri, M. R. *et al.* The wet precipitation process of hydroxyapatite. *Mater. Lett.* **57**, 4064–4069 (2003).
33. Afshar, A. *et al.* Some important factors in the wet precipitation process of hydroxyapatite. *Materials and Design.* **24**, 197–202 (2003).
34. Bezzi, G. *et al.* A novel sol-gel technique for hydroxyapatite preparation. *Materials Chemistry and Physics.* **78**, 816–824 (2003).
35. Wang, Y. J. *et al.* Surfactant-assisted synthesis of hydroxyapatite particles. *Mater. Lett.* **60**, 3227–3231 (2006).
36. Wang, Y. *et al.* Hydrothermal synthesis of hydroxyapatite nano-powders using cationic surfactant as a template. *Mater. Lett.* **60**, 1484–1487 (2006).
37. Panda, R. N. *et al.* FTIR, XRD, SEM and solid state NMR investigations of carbonate-containing hydroxyapatite nano-particles synthesised by hydroxide-gel technique. *J. Physics and Chemistry of Solids.* **64**, 193–199 (2003).
38. Farzadi, A., Solati-Hashjin, M., Bakhshi, F. & Aminian, A. Synthesis and characterization of hydroxyapatite/β-tricalcium phosphate nano-composites using microwave irradiation. *Ceramics International.* **37**, 65–71 (2011).
39. Bancroft, J. D. & Gamble, M. *Theory and practice of histology techniques* (Churchill Livingstone, London, 2002).
40. Junqueira, L. C. U. *et al.* Differential histological diagnosis of osteoid. *Journal of Pathology.* **148**, 189–196 (1986).
41. Poinern, G. E. J. *et al.* Synthesis and characterisation of nanohydroxyapatite using an ultrasound assisted method. *Ultrasonics Sonochemistry.* **16**, 469–474 (2009).
42. Poinern, G. E. J. *et al.* Thermal and ultrasonic influence in the formation of nanometre scale hydroxyapatite bio-ceramic. *International Journal of Nanomedicine.* **6**, 2083–2095 (2011).
43. Dorozhkin, S. V. Medical application of calcium orthophosphate bioceramics. *BIO.* **1**, 1–51 (2011).
44. Webster, T. J. *et al.* Enhanced osteoclast-like cell functions on nanophase ceramics. *Biomaterials.* **22**, 1327–1333 (2001).
45. Detch, R. *et al.* The resorption of nanocrystalline calcium phosphates by osteoclast-like cells. *Acta Biomater.* **6**, 3223–3233 (2010).
46. Koerten, H. & van der Meulen, J. Degradation of calcium phosphate ceramics. *J. Biomed. Mater. Res.* **44**, 78–86 (1999).
47. Li, S. *et al.* The effects of sintering temperature and pressure on the sintering behaviour of hydroxyapatite powder prepared by spark plasma sintering. *J. Biomech. Sci. Eng.* **3**, 1–12 (2008).
48. Despang, F. *et al.* Synthesis and physicochemical, in vitro and in vivo evaluation of an anisotropic, nanocrystalline hydroxyapatite bisque scaffold with parallel-aligned pores mimicking the microstructure of cortical bone. *J. Tissue. Eng. Regen. Med.* DOI:10.1002/term.1729 (2013).
49. Tadica, D. *et al.* A novel method to produce hydroxyapatite objects with inter-connecting porosity that avoids sintering. *Biomaterials.* **25**, 3335–3340 (2004).
50. Galois, L. & Mainard, D. Bone in growth into two porous ceramics with different pore sizes: an experimental study. *Acta Orthop. Belg.* **70**, 598–603 (2004).
51. Cunningham, E. *et al.* High solid content hydroxyapatite slurry for the production of bone substitute scaffolds. *Proc. IMechE. HJ. Eng. Med.* **223**, 727–737 (2009).
52. Landi, E. *et al.* Carbonated hydroxyapatite as bone substitute. *J. Eur. Ceram. Soc.* **23**, 2911–2937 (2003).
53. Lonnissa, H. *et al.* Vascularized bone tissue engineering: approaches for potential improvement. *Tissue Eng Part B Rev.* **18**, 363–382 (2012).

54. Aichmair, A. *et al*. Symptomatic heterotopic bone formation after rhBMP-2 utilization in lateral lumbar interbody fusion. *The Spine Journal*. **13**, 1411; DOI: 10.1016/j.spine.2013.07.473 (2013).
55. Luo, X. *et al*. Zinc in calcium phosphate mediates bone induction: in vitro and in vivo model. *Acta Biomateriala*. **10**, 477–485 (2014).
56. Poinern, G. E. J., Brundavanam, R. K., Le, X. & Fawcett, D. The mechanical properties of a porous ceramic derived from a 30 nm sized particles based powder of hydroxyapatite for potential hard tissue engineering applications. *Am. J. Biomed. Eng.* **2**, 278–286 (2012).

Acknowledgments

Dr Derek Fawcett would like to thank the Bill & Melinda Gates Foundation for their research fellowship. The authors would like to acknowledge the assistance of G. Spoelstra and M. Slaven for preparing tissue samples for optical microscopy. The authors would also like to thank I. Pitout for the surface image of the ceramic pellet, and both Prof. Arie Van Riessen and Zhenhua Luo of Curtin University for undertaking the hardness testing.

Author contributions

G.E.J.P., R.K.B. and D.F., conceived the idea and designed the experimental. R.K.B. and X.L. performed materials experimental work and carried out materials characterization measurements. M.A.C. performed the *in vivo* experiments, while P.K.N. performed the histology analysis. G.E.J.P., R.K.B., X.L. and D.F. analyzed the data and wrote the manuscript. D.F. and X.L. prepared the figures. All authors reviewed the manuscript.

Additional information

Supplementary information accompanies this paper at http://www.nature.com/scientificreports

Competing financial interests: The authors declare no competing financial interests.

How to cite this article: Poinern, G.E.J. *et al*. The synthesis, characterisation and *in vivo* study of a bioceramic for potential tissue regeneration applications. *Sci. Rep.* **4**, 6235; DOI:10.1038/srep06235 (2014).

This work is licensed under a Creative Commons Attribution-NonCommercial-NoDerivs 4.0 International License. The images or other third party material in this article are included in the article's Creative Commons license, unless indicated otherwise in the credit line; if the material is not included under the Creative Commons license, users will need to obtain permission from the license holder in order to reproduce the material. To view a copy of this license, visit http://creativecommons.org/licenses/by-nc-nd/4.0/